scientific reports

Check for updates

OPEN

Synergistic mechanisms of temperature and strain rate on plastic deformation in SLM 3D printed SS316L utilizing hot processing map analysis

Ambuj Saxena[1], Shashi Prakash Dwivedi[2], Shubham Sharma[3,4,5]✉, Neeraj Mishra[6], Tarun Kumar Gupta[1], N. Beemkumar[7], Ankit Kedia[8], V. Nagabhushana Rao[9], Ehab El Sayed Massoud[10], Dražan Kozak[11] & Jasmina Lozanovic[12]✉

The plastic deformation behavior of selective laser melting (SLM) 3D printed SS316L steel has been analyzed at the temperature range 25- 1000℃ (25 (room temperature), 200, 400, 600, 800 and 1000℃) and strain rate range 10^{-3}-$10^{3}s^{-1}$ (10^{-3}, 10^{-2}, 10^{-1}, 10^{0}, 10^{1}, 10^{2} and 10^{3} s^{-1}) under compressive loading environments. The flow stress vs. plastic strain results revealed that the flow stress was reduced 136.64% from room temperature to 1000℃ at $10^{-3}s^{-1}$. Further, the flow stress was decreased 102.86% from room temperature to 1000℃ at $10^{3}s^{-1}$. The flow stress was increased 46.63% from $10^{-3}s^{-1}$ to $10^{3}s^{-1}$ at room temperature. Moreover, the flow stress was increased 95.07% from $10^{-3}s^{-1}$ to $10^{3}s^{-1}$ at 1000℃. The temperature and strain rate effect on strain rate sensitivity (m) has been observed for SLM 3D printed SS316L steel. Based on strain rate sensitivity (m), the power dissipation efficiency (η) and instability dimensionless parameter ($\xi\ (\dot{\epsilon})$) map plot contours have been investigated under various hot working parameters for SLM 3D printed SS316L steel. Further, hot working processing maps have been generated by superimposing instability dimensionless parameters ($\xi\ (\dot{\epsilon})$) map on the power dissipation efficiency (η) map for SLM 3D printed SS316L steel. The processing map was further related with investigated material microstructure to identify the hot processing safe and unsafe zone for SLM 3D printed SS316L. The unsafe instability region occurred at the low strain rate range (10^{-2} – 10^{-1} s^{-1}), high strain rate range (10^{2}-10^{3} s^{-1}) and temperature range (200–400℃, and 800 – 100℃) for 0.02, 0.04, 0.06, 0.08 and 0.10 strain. Further, the remaining area was useful for hot workability. The Vicker's hardness revealed that the hardness was decreased with 3.87%, 12.55%, 22.01%, 32.35%,

[1]Department of Mechanical Engineering, G. L. Bajaj Institute of Technology and Management, Greater Noida 201306, India. [2]Department of Mechanical Engineering, Lloyd Institute of Engineering and Technology, Greater, Noida, India. [3]Department of Technical Sciences, Western Caspian University, Baku, Azerbaijan. [4]Centre for Research Impact and Outcome, Chitkara University Institute of Engineering and Technology, Chitkara University, Rajpura 140401, Punjab, India. [5]Jadara University Research Center, Jadara University, Irbid, Jordan. [6]Center for Artificial Intelligence and Robotics, Madhav Institute of Technology & Science, Gwalior 474005, India. [7]Department of Mechanical Engineering, School of Engineering and Technology, JAIN (Deemed to Be University), Bangalore, Karnataka, India. [8]Department of Mechanical & Aerospace Engineering, NIMS Institute of Engineering & Technology, NIMS University Rajasthan, Jaipur, India. [9]Department of Mechanical Engineering, Raghu Engineering College, Vishakhapatnam 531162, Andhra Pradesh, India. [10]College of Applied Sciences, King Khalid University, Dhahran Al-Janoub, Kingdom of Saudi Arabia. [11]Mechanical Engineering Faculty in Slavonski Brod, University of Slavonski Brod, Trg Ivane Brlić-Mažuranić 2, Slavonski Brod HR-35000, Croatia. [12]Department of Engineering, FH Campus Wien - University of Applied Sciences, 1100 Vienna, Austria. ✉email: shubham543sharma@gmail.com; shubhamsharmacsirclri@gmail.com; jasmina.lozanovic@fh-campuswien.ac.at

and 43.70% at 200^{0}C, 400^{0}C, 600^{0}C, 800^{0}C and 1000^{0}C respectively with respect to room temperature hardness.

Keywords Selective laser melting (SLM), 3D printing, SS316L steel, Strain rate sensitivity (m), Plastic flow behavior, Power dissipation efficiency (η) map, Processing map, Instability dimensionless parameter ($\xi\ (\dot{\epsilon})$) map, Vicker's hardness

Abbreviation

σ	True stress
A_{bar}	cross-section area of the bar
A_{Sp}	cross-section area of the specimen
E_{bar}	Young's modulus of the bar
$\dot{\epsilon}_l$	loading strain rate
c_{bar}	longitudinal stress wave velocity
ρ_{bar}	density of the bar
P	dissipated power
G	dissipation capacity generated by the specimen's temperature rise during plastic deformation
j	dissipation capacity generated by the metallurgical processes during the plastic deformation
$\dot{\epsilon}$	Strain rate
m	Strain rate sensitivity
η	power-dissipation efficiency
$\xi\ (\dot{\epsilon})$	Flow instabilities dimensionless parameter
T	Temperature

The 3D printing is an advanced manufacturing technique in which the material builds layer by layer to create complex geometry objects[1,2]. The selective laser melting (SLM) 3D printed SS316L steel objects have been utilised mostly in compressive environments due to their good mechanical properties like high yield strength, compressive strength, ductility and corrosion resistance[3,4]. The SS316L steel is a low-carbon variant and is mostly used in biomedical applications due to its exceptional properties. The high corrosion resistance property against bodily fluids and saline environments makes it useful in developing surgical tools. Further, the biocompatibility of SS316L minimizes adverse reactions with blood and tissues. The non-magnetic nature of SS316L makes it compatible with MRI procedures and reduces risk during imaging[5–7]. The widely used technique for metal 3D printing is Selective Laser Melting (SLM) due to its ability to produce metal parts with exceptional precision, density, and mechanical properties. The SLM supports near-net-shape production and minimizing material waste, which is particularly advantageous when working with expensive metals like titanium or stainless steel. Further, the SLM process provides good control over the microstructural characteristics of printed parts by fine-tuning process parameters such as laser power, scan speed, and layer thickness. The mentioned microstructural control enables the production of tailored mechanical properties for use in aerospace, biomedical, and automotive industries, where performance and reliability are critical[8–10].

The 3D SLM printed parts have been utilized in biomedical implants, high-pressure environments and structural components where compressive loading is crucial[5–7]. Further, the study of workability at elevated temperatures for SLM 3D printed objects is useful to component design for aerospace, automotive, and energy industries[8–10]. The mechanical processing and workability of SLM 3D printed objects are influenced by microstructure, temperature, strain, strain rate and stress rate in the deformation zone[11,12]. Further, the material deformation was enhanced by the application of external hydrostatic slow-speed compression with a stable fine-grained structure at higher temperatures[13,14]. The processing map is the technique used to analyse the workability of an SLM 3D printed material deformed under specific strain, strain rate, and temperature without showing flow instability and cracks[12]. Further, processing maps provide a visual depiction of the SLM 3D printed material deformation behaviour with microstructural changes and notify the effectively and safely processed regions. Moreover, in the safely processed regions SLM 3D printed material exhibited stable, ductile flow indicating optimal workability[12,13]. The processing maps also indicate the instability zones (poor workability) where processing conditions lead to defects and undesirable microstructures. The processing maps help optimize manufacturing parameters for provide a formed-shaped to SLM 3D printed material without compromising its structural integrity. Further, the processing map study enhanced the quality and performance of the product. Hence, the processing map describes certain and uncertain regions for the allowed and avoided mechanical processing respectively. Moreover, processing maps provide the optimal mechanical processing strain rate and temperature.

Venugopal et al.[11] developed the processing map for the AISI 316 L steel at a temperature range of 600–1250^0 C and strain rate range of 0.001–100 s^{-1}. Further, the results revealed that the peak efficiency of power dissipation was achieved as 35% at the 0.05 s^{-1} strain rate and 1250^{0}C. Pu et al. [12] studied the hot deformation behavior of superaustenitic stainless steel S32654 at the temperature range of 950–1250^0 C and strain rate range of 0.001–10 s^{-1} and developed a processing map for the same. Further, the result revealed that the peak efficiency of 49% was obtained in the temperature regime 1030–1150^0 C and strain rate range 0.01–0.04 s^{-1}. Wu et al.[13] investigated the aluminium content influence on the hot deformation behaviour of Fe-Mn-Al-C steels with the help of hot processing maps at the temperature range of 850–1050 °C and strain rate range of 0.001–10 s^{-1}. Further, the result exhibited that high Al content weakens the workability of the Fe-Mn-Al-C steels. Mohamadizadeh et al.[14] developed the hot processing maps for duplex low-density Fe-18Mn-8Al-0.8 C steel at 600–1000 °C temperature range and strain rate range of 0.001–10 s^{-1}. Further, the safe efficiency zone was found

at the 700–900^0 C temperature range with the strain rate range of 0.1–1 s^{-1}. Further, a similar type of study has been performed by Pu et al.[12] on the super austenitic stainless steel S32654. Further, the maximum efficiency was achieved at 1030–1150^0 C temperature and 0.01–0.4 s^{-1} strain rate.

The above-mentioned literature review reveals that the workability and hot deformation analysis for additively manufactured SLM 3D-printed material are rarely available in the existing literature. Hence a clear gap exists in the understanding of hot deformation workability analysis of additively SLM 3D-printed SS316L stainless steel through processing maps. The power dissipation efficiency (η) and Instability dimensionless parameter ($\xi\ (\dot{\epsilon})$) maps are not available for the SLM 3D-printed SS316L stainless steel in the literature.

In the present investigation, the processing maps, power dissipation efficiency (η) and Instability dimensionless parameter ($\xi\ (\dot{\epsilon})$) maps have been developed to estimate the safely processed and the instability regions during workability for SLM 3D-printed SS316L steel at 0.1–10^3 s^{-1} strain rate range and 25–1000℃ temperature range. The processing maps has been developed with the low and high strain rate compression testing experimental results. Further, the investigation has also been revealed the specific strain, strain rate, and temperature without showing flow instability and cracks at the time of SLM 3D printed SS316L steel deformation. The influence of temperature on SLM 3D printed SS316L steel Vicker's hardness has also been investigate. Finally, the microstructure investigation has also been carried out to understand the deformation mechanism of SLM 3D printed SS316L steel.

Experimental methodology

A systematic approach was followed to develop the hot working processing maps for SLM 3D-printed SS316L steel as shown in the flowchart (Fig. 1). The first step of methodology begins with the SLM printing of SS316L low and high strain rate testing specimens for the performing of different experiments to accomplish the objective. In the second step, the high and low strain rate compression testing was performed with the help of a universal testing machine (UTM) and split-Hopkinson pressure bar respectively at the temperature range of room temperature to 1000^{0}C. In the third step, data collection of experimental testing and flow stress vs. plastic strain analysis was performed for the under-investigated material. In the fourth step, strain rate sensitivity analysis (m) was done at the temperature range 25 to 1000^{0}C. In the Fifth step, Power dissipation efficiency (η) map was generated to identify the safe deformation zones in processing maps, guiding hot working conditions (e.g., temperature & strain rate) for achieving desirable microstructures. The sixth step deals with the development of the Instability dimensionless parameter (($\xi\ (\dot{\epsilon})$)) map. The instability dimensionless parameter (($\xi\ (\dot{\epsilon})$)) can help in selecting the best thermal-mechanical processing conditions to enhance ductility and strength. In 7th step hot processing map was developed by overlapping power dissipation efficiency (η) map and Instability dimensionless parameter (($\xi\ (\dot{\epsilon})$)) map. The hot processing map is a crucial tool for optimizing the hot deformation behavior of materials by identifying stable and unstable regions based on temperature and strain rate. It helps to define the safe processing zones.

The microstructure investigation of SLM 3D printed SS316L samples was presented in 8th step at 1000^{0}C. In the last step (9th step) the Vicker's hardness of developed SLM 3D printed SS316L samples at the temperature range of room temperature to 1000^{0}C.

Selective laser melting (SLM)

A high-powered laser has been utilised to melt the fine metal powders and build the required object layer by layer in selective laser melting (SLM) 3D printing. A computer-aided design file of the required object has been saved into .stl file format for 3D printing. Further, .stl file format sliced geometry into layers and translated it into machine instructions. A laser beam melts and fuses the thin layer of SS316L metal powder particles which thin layer spreads on the build platform. Further, the laser also traces the cross-sectional geometry to form the entire part. Figure 2 (a) revealed a powder bed fusion process which used a high-intensity laser beam to melt and fuse the SS316L steel powder to build the object layer by layer. DMP Flex 2000 3D printer (Manufacturer: 3D systems) with 140 × 140 × 115 mm build volume has been utilized to 3D print the SS316 L compression and split Hopkinson pressure bar test specimens in the vertical direction (shown in Fig. 2 (b)). SS316L steel powder was used to print the low and high-strain rate compression samples. The investigated material SS316 L powder objects were biocompatible with human tissues without negative effects. In the current investigation, 40 to 60 µm particle size SS316 L powder was utilised. The chemical composition of SS316L has been mentioned in Table 1. The process parameters for SLM 3D printing of compression test specimens are mentioned in Table 2.

Low strain rate compression testing, high strain rate compression testing and hardness testing

Low strain rate compression tests were performed on SLM 3D-printed SS316L specimen by utilizing a Walter + Bai Ag universal testing machine over a 10^{-3} to 10^0 strain rate range and 25℃ to 1000℃ temperature range. The cylindrical sample size for low strain rate compression testing was 5 mm in diameter and 10 mm in length. The 3D printed SS316L samples for low strain rate UTM compression testing and high strain rate SHPB compression testing are shown in Fig. 2 (c) and Fig. 2 (d) respectively. The load compression data was converted to true stress vs. true strain curve data. Further, the high strain rate compression tests were performed on a split-Hopkinson pressure bar (SHPB) setup with the strain rate range 10^2–10^3 s^{-1} and 25℃ to 1000℃ temperature range. The dimension of the SHPB set up has been shown in Fig. 3. In the SHPB test process the striker bar impacted on the incident bar with an initial axial velocity V. Further, this impact formed a trapezoidal incident stress impulse wave in the incident bar and then into the specimen. A portion of the incident stress impulse wave is transmitted to the transmitted bar through the specimen. The balance portion is reflected into the incident bar back due to material mismatch as shown in Fig. 3. The pulse characteristic is varied with the variation in striker bar length.

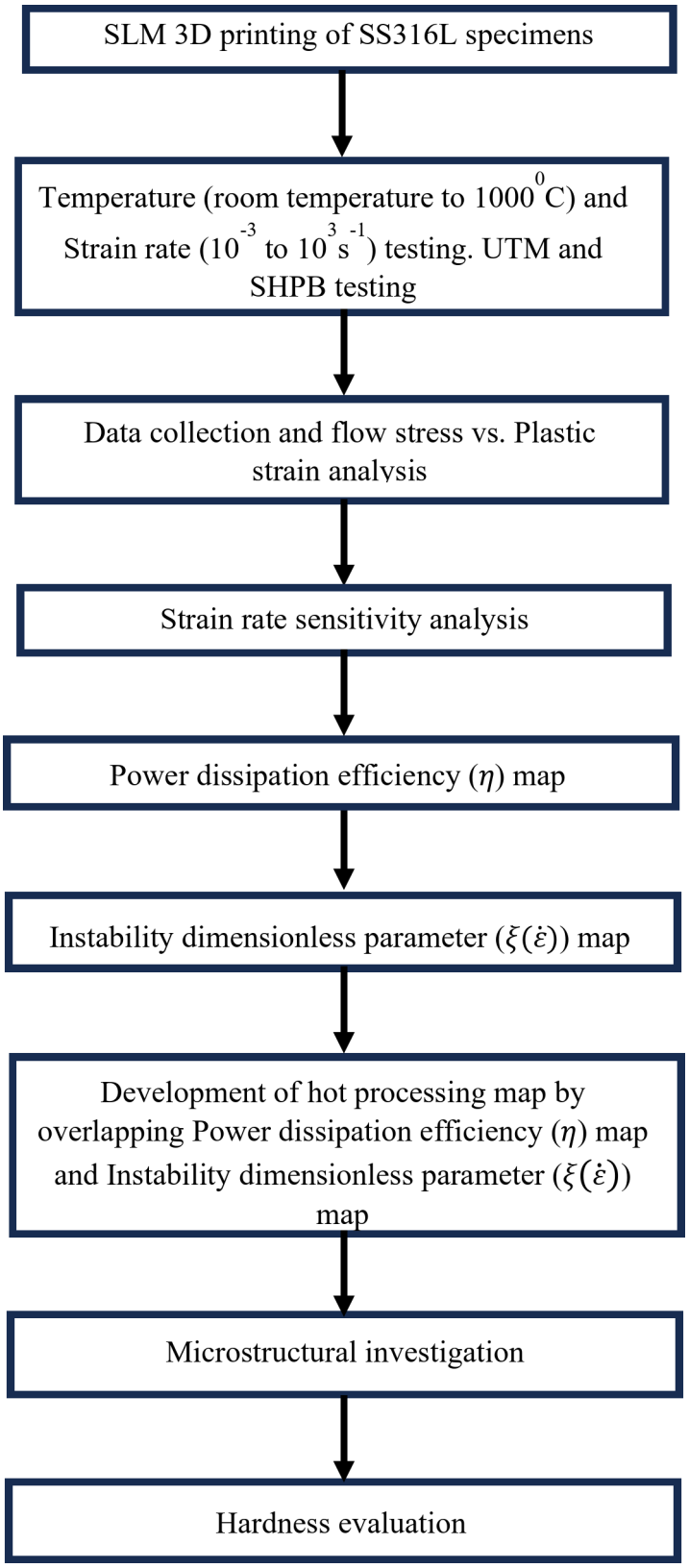

Fig. 1. Methodology layout of the current investigation.

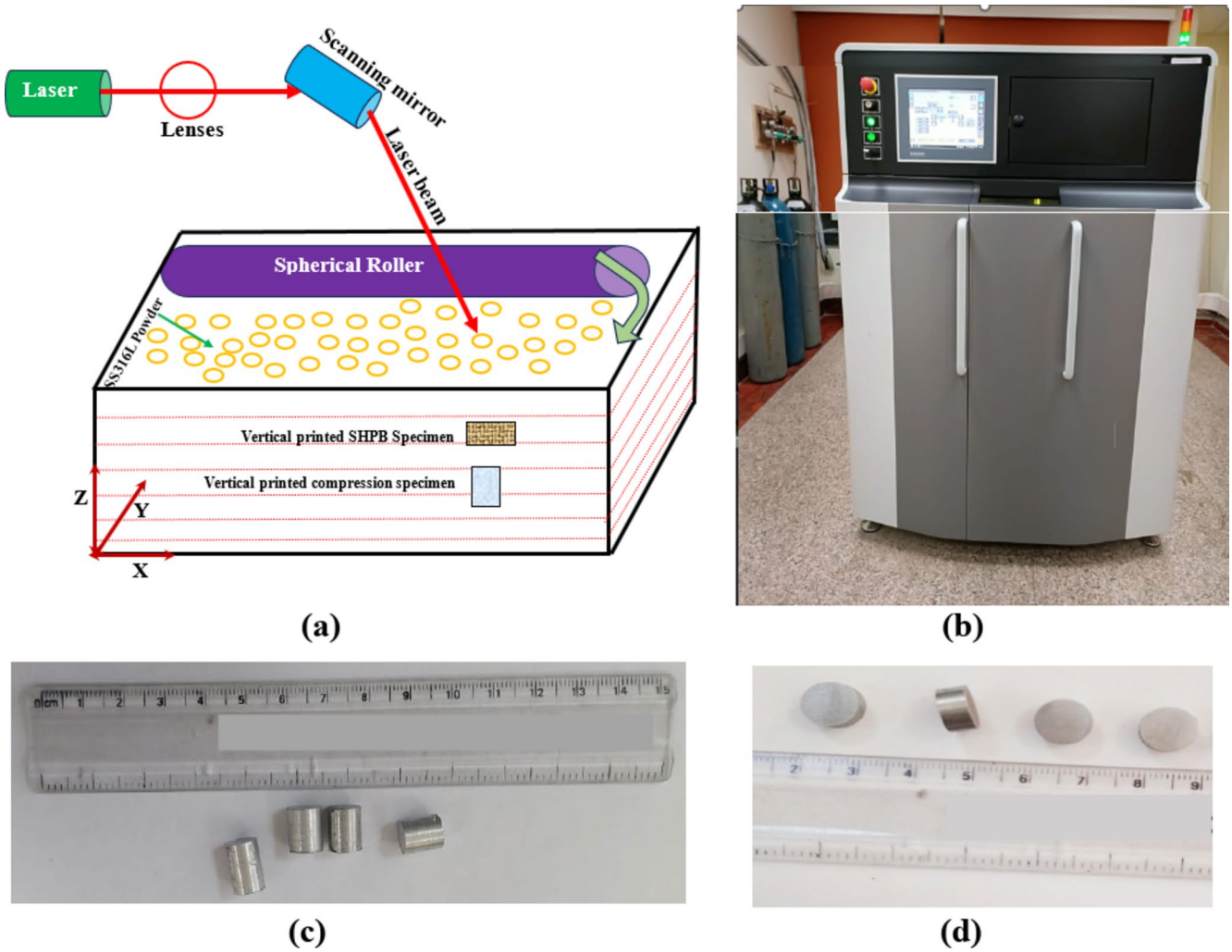

Fig. 2. (**a**) Selective laser melting (SLM) 3D printing schematic diagram, (**b**) DMP Flex 3D printer, (**c**) 3D printed low strain rate compression test samples for UTM compression test, (**d**) 3D printed high strain rate compression samples for SHPB test [The figures are completely original and thus, there is no need to remove the main identifiers].

Elements	Cr	Ni	Mo	C	*N*	Fe
Weight% (%)	18	14	2.25	0.03	0.10	Balance

Table 1. Chemical composition of SS316L.

Process Parameters	Value
Laser power (W)	190
Scanning speed (m/s)	0.8
Hatch spacing (μm)	120
Layer thickness (μm)	50

Table 2. Process parameters used in 3D printing.

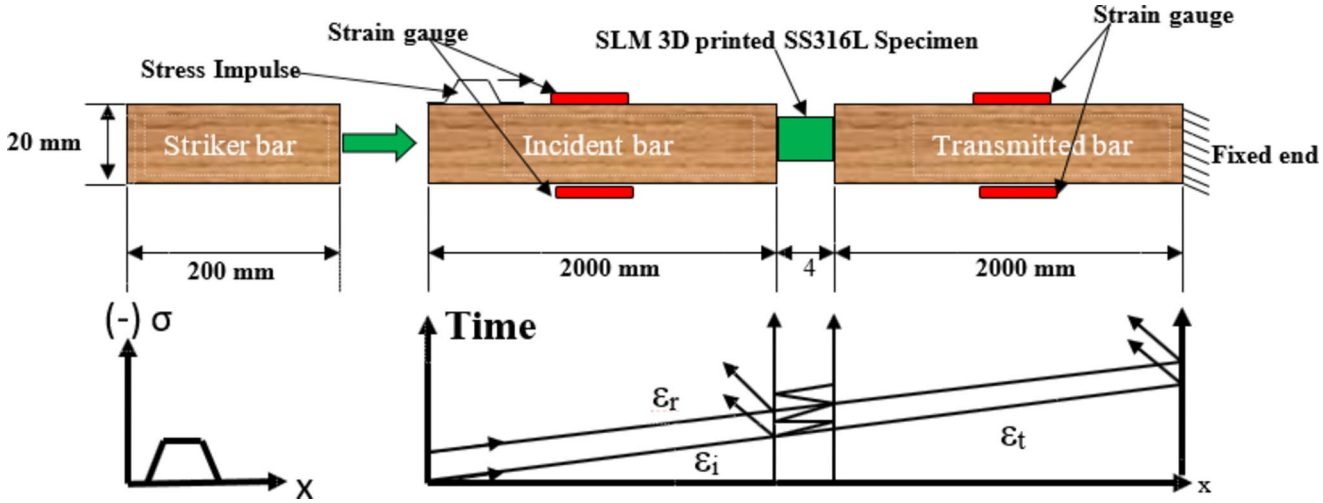

Fig. 3. Schematic diagram of SHPB setup.

The dimensions of the cylindrical specimen for the SHPB test are 8 mm in diameter and 4 mm in length. The relationship between the incident reflected, and the transmission bar signals are mentioned below in Eq. (1)[15]:

$$\epsilon_i = \epsilon_t + \epsilon_r \tag{1}$$

Where, ε_i, ε_r, and ε_t are the incident, reflected, and transmitted signals in the bars respectively.

The true stress, true strain, and strain rate of the SLM 3D printed specimen were evaluated based on a one-dimensional assumption with the help of Eqs. (2), (3) and (4) respectively[16].

$$\sigma = \frac{A_{bar} E_{bar} \epsilon_t}{A_{sp}} \tag{2}$$

$$\epsilon = \int_0^t \dot{\epsilon_l}\, \mathrm{dt} \tag{3}$$

$$\dot{\epsilon_l} = \frac{2 c_{bar} \epsilon_r}{L} \tag{4}$$

where A_{bar}=cross-section area of the bar, A_{sp} = cross-section area of the specimen, E_{bar}= Young's modulus of the bar, $\dot{\epsilon_l}$ = loading strain rate, c_{bar} = longitudinal stress wave velocity.

The c_{bar} was evaluated with the following Eq. (5):

$$c_{bar} = \sqrt{\frac{E_{bar}}{\rho_{bar}}} \tag{5}$$

Where ρ_{bar} is the density of the bar.

The Vicker's hardness test was conducted on a Vicker's hardness tester at room temperature, 200^{0}C, 400^{0}C, 600^{0}C, 800^{0}C, and 1000^{0}C[26]. The applied load was kept at 0.5 kg for 10 s to perform the hardness testing. Further, the dimension of the Vicker's hardness testing specimen was considered as 25 × 25 × 12.5 mm.

Hot processing maps: analytical modelling and formation

The combination of the instability map and power dissipation efficiency map generates the processing map. Further, the processing maps were established to overlap the instability map on the power dissipation efficiency map. The processing map is based on the dynamic material model (DMM).

The specimen on which hot working was processed, consumes the energy during the plastic deformation. Further, the first type of consumed power is dissipation capacity (G) generated by the specimen's temperature rise during plastic deformation. Moreover, the second type of heat is dissipation capacity (J) generated by the metallurgical processes during the plastic deformation. The dissipated power (P) can be expressed in terms of G and J with the help of the following Eq. (6)[16]:

$$P = \sigma\, \dot{\epsilon} = \int_0^{\dot{\epsilon}} \sigma\, d\dot{\epsilon} + \int_0^{\sigma} \dot{\epsilon}\, d\sigma = G + J \tag{6}$$

Further, the relation between G and J can be expressed by Eq. (7) as follows:

$$\frac{dJ}{dG} = \frac{\dot{\epsilon}\, d\sigma}{\sigma\, d\dot{\epsilon}} = \frac{d\, log\sigma}{d\log\dot{\epsilon}} = m \tag{7}$$

Where m is the strain rate sensitivity, the relation between the flow stress and stress rate sensitivity is expressed with the Eq. (8):

$$\sigma = K\dot{\epsilon}^{\,m} \tag{8}$$

The Eq. (8) is known as the dynamic constitutive equation and the value can be evaluated with the help of flow stress value at the different strain rates.

The value of J can be derived with the help of Eq. (6) and the new expression can be written as mentioned in Eq. (9):

$$J = P - G = \sigma\,\dot{\epsilon} - \int_0^{\dot{\epsilon}} \sigma\, d\dot{\epsilon} \tag{9}$$

The value of σ put into the Eq. (9) from the Eq. (8). Further, Eq. (9) is changed into Eq. (10) and can be expressed as follows:

$$J = P - G = \sigma\,\dot{\epsilon} - \int_0^{\dot{\epsilon}} K\dot{\epsilon}^{\,m} d\dot{\epsilon} = \frac{m}{m+1}\,\sigma\,\dot{\epsilon} \tag{10}$$

The ideal linear dissipation process has occurred at m = 1, then the Eq. (11) expressed the maximum value of J:

$$J_{maximum} = J\ (m+1) = \frac{1}{2}\sigma\,\dot{\epsilon} \tag{11}$$

Further, the ratio of Eq. (10) and Eq. (11) represents the power-dissipation efficiency (η)[17,18]. The Eq. (12) shows the expression for the power-dissipation efficiency (η) :

$$\eta = J = \frac{J}{J_{\,maximum}} = \frac{2m}{m+1} \tag{12}$$

Equation (12) revealed that the power dissipation efficiency (η) is dependent on the strain rate sensitivity (m) directly.

The condition of flow instabilities for material deformation is expressed according to one dimensionless parameter ($\xi\ (\dot{\epsilon})$) with the following Eq. (13)[19,20]:

$$\xi\ (\dot{\epsilon}) = \frac{\partial\, log\left(\frac{m}{m+1}\right)}{\partial\, ln\dot{\epsilon}} + m < 0 \tag{13}$$

Further, Eq. (13) exhibited that the flow instability condition also depends on the strain rate sensitivity (m).

The two-dimensional hot processing instability map is generated through the variation of $\xi\ (\dot{\epsilon})$ with the strain rate $(\dot{\epsilon})$ and temperature (T). Further, the negative $\xi\ (\dot{\epsilon})$ region of a two-dimensional hot processing instability map shows the microstructure instabilities.

Hence, the processing maps were established to overlap the instability map on the power dissipation efficiency map.

Result and discussion

Effect of temperature and strain rate on the plastic flow behavior of SLM 3D printed SS316L steel

Figure 4 exhibited the effect of temperature and strain rate on the flow stress vs. plastic strain curve for SLM 3D printed SS316L steel printed specimen at the 25 (room temperature) to 1000℃ temperature range and 10^{-3} to 10^{3} s^{-1} strain rate range up to 10% of plastic strain. The graph revealed that the flow stress continuously decreased with the increase in temperature from 25 to 1000℃ for SLM 3D printed SS316L steel.

Further, the main reason behind the reduction of flow stress is the thermal activation process which also decreases the deformation resistance ability. The atomic vibrations within the investigated material increase at the high temperature. Further, the increased atomic vibration increases the dislocation movement through the crystal lattice. Moreover, the increase in dislocation movement reduces the SLM 3D printed SS316L steel yield strength and ultimate tensile strength. The recrystallization mechanisms also occur at elevated temperatures in SLM 3D-printed SS316 steel leading to low flow stress. Figure 4 also revealed that the flow stress is increased with the strain rate throughout the temperature range of 25 (room temperature) to 1000℃ for SLM 3D printed SS316L steel. At the high strain rate less, time is available for the dislocation movement and dislocation rearrangement within the crystal lattice. The less dislocation movement leads to the accumulation of dislocations which results in the formation of internal barriers for further dislocation movement and increases the resistance to deformation[21].

Table 3 shows the comparison of present investigation additive manufactured sample result with the existing literature additive manufacturing sample results at the high strain rate ($10^{3}s^{-1}$) and room temperature. Further,

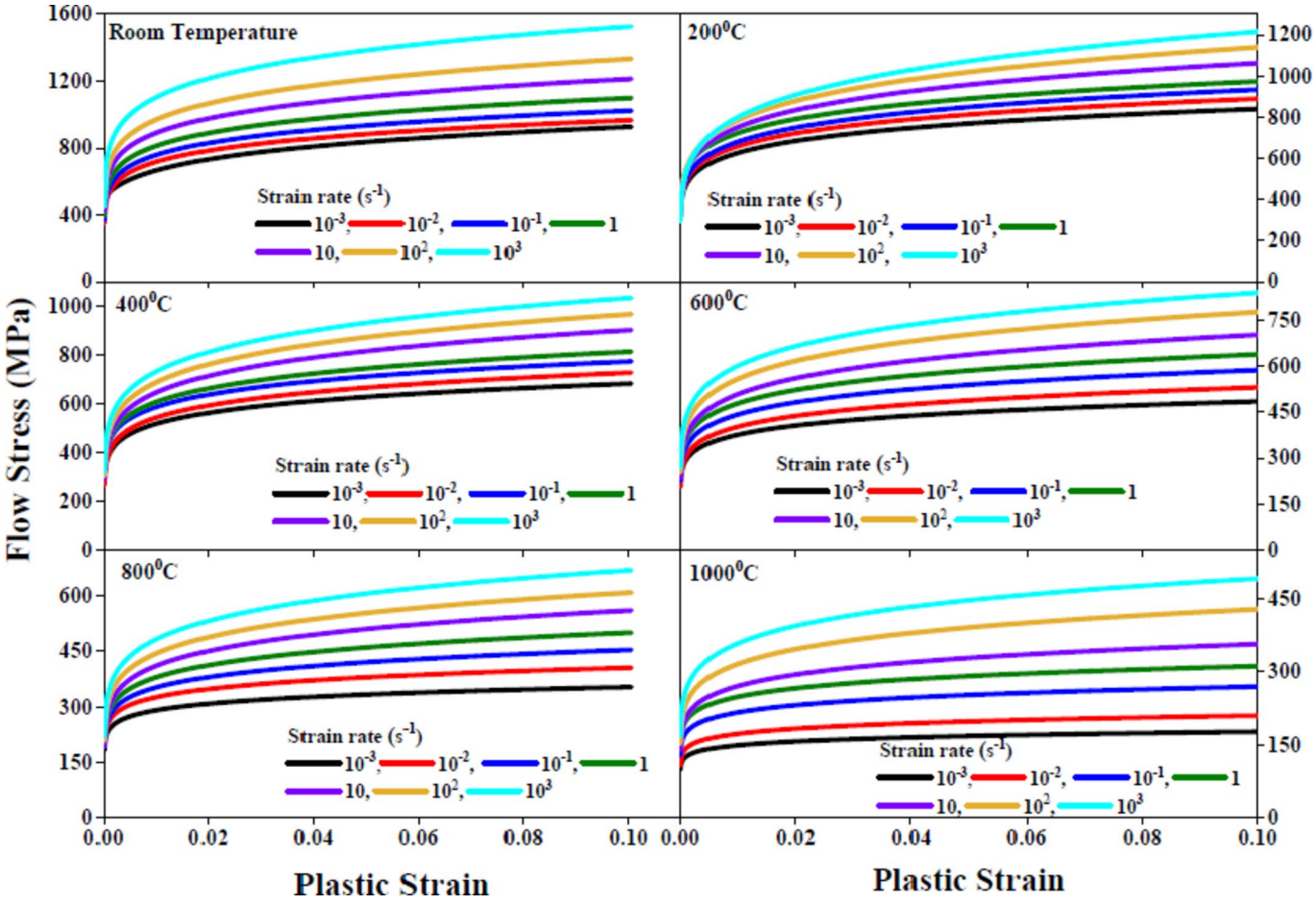

Fig. 4. Flow stress vs. Plastic strain curve for SLM 3D printed SS316L steel at the temperature range 25℃ to 1000℃ and strain rate range 10^{-3} to 10^{3} s^{-1}.

Investigation at room temperature	Maximum Stress (MPa)
Current Investigation at 5×10^3 s^{-1} strain rate (Sample prepared with Selective laser melting additive manufacturing technique)	1496.24
Bevan et al. [22] at 2.2×10^3 s^{-1} strain rate (Sample prepared with Laser Powder Forming additive manufacturing technique)	1398.10 (6.76% difference)
Ziętala et al. [23] at 4×10^3 s^{-1} strain rate (Sample prepared with Laser Engineered Net Shaping (LENS) additive manufacturing technique)	1198.23 (22.12% difference)
Ziętala et al. [23] at 4×10^3 s^{-1} strain rate (Wrought Sample)	1530.32 (2.25% difference)
Chen et al. [24] at 4.32×10^3 s^{-1} strain rate (Sample prepared with cold metal transfer (CMT) process additive manufacturing technique)	1605.21 (7.02% difference)
Chen et al. [24] at 3.250×10^3 s^{-1} strain rate (Wrought Sample)	1702.12 (12.87% difference)
Kneen et al. [25] at 2.739×10^3 s^{-1} strain rate (Sample prepared with Selective laser melting additive manufacturing technique)	1195 (22.38% difference)
Kneen et al. [25] at 2.739×10^3 s^{-1} strain rate (Wrought Sample)	1368 (8.95% difference)

Table 3. Comparison between the present investigation and existing literature.

the results revealed that the percentage difference between existing literature and current investigation is varies from 6.76 to 22.38%. The less percentage difference between values shows the accuracy of measuring values[27,28].

Effect of temperature, strain and strain rate on the strain rate sensitivity (m)

In the process of developing processing maps, the power dissipation efficiency (η) and flow instabilities dimensionless parameter (ξ ($\dot{\epsilon}$)) both depend on the strain rate sensitivity (m). The strain rate sensitivity (m) was evaluated with the help of Eq. (7).

Figure 5 shows the graphs between Ln (σ) vs. Ln ($\dot{\epsilon}$) the at the 25 (room temperature) to 1000℃ temperature range and 0.02, 0.04, 0.06, 0.08 and 0.10 plastic strain. The results revealed that at a particular plastic strain, flow

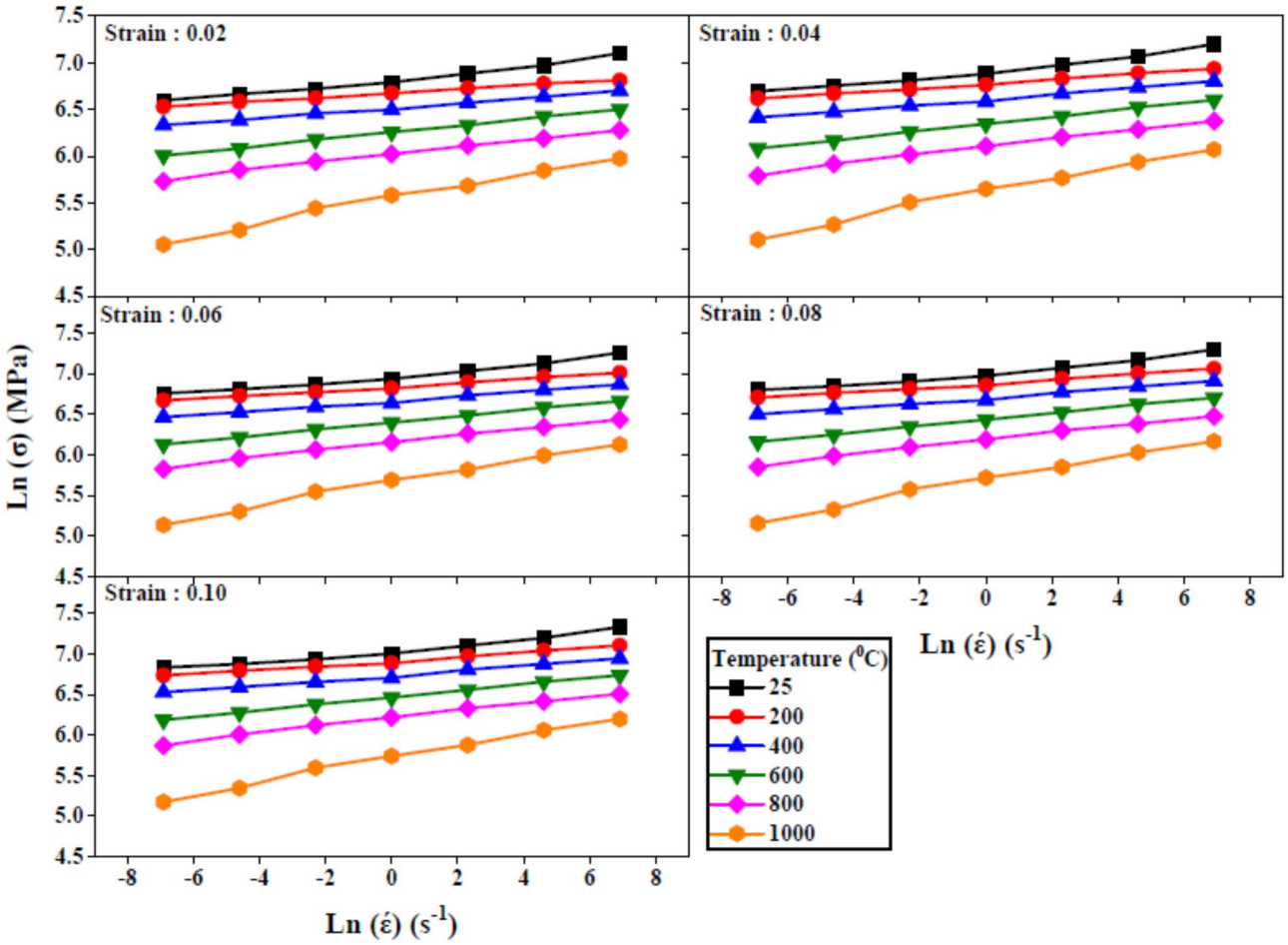

Fig. 5. Ln (σ) vs. Ln $(\dot{\epsilon})$ for SLM 3D printed SS316L steel at the temperature range 25 to 1000^0C and 0.02, 0.04, 0.06, 0.08 and 0.10 plastic strain. Flow stress vs. Plastic strain curve for SLM 3D printed SS316L steel at the temperature range 25℃ to 1000℃ and strain rate range 10^{-3} to 10^3 s^{-1}.

stress is increased with the increased in strain rate at all the temperatures. The derivatives of Ln (σ) vs. Ln $(\dot{\epsilon})$ curve derived the m value at a given strain and temperature. Figure 6 shows the variation in stress rate sensitivity with a 25 (room temperature) to 1000^0C temperature range and 0.02 to 0.10 strain. Figure 6 was driven from the Fig. 5 and Eq. (7).

Further, the results revealed that the strain rate sensitivity (m) of the investigated material was increased with the increase in the temperature at each plastic strain value (0.02, 0.04, 0.06, 0.08 and 0.10). Further, a small variation was observed in m values at the 25 (room temperature) to 400℃ temperature range. Moreover, a significant variation in m values was noticed for the temperature range 600℃ to 1000℃. The increase in temperature increases the thermal energy in the material and leads to dislocation mobility. Further, the enhanced dislocation movement activates the thermally driven process of diffusion, dynamic recovery, and recrystallisation, which causes deformation accommodation in the investigated material. Further, the grain boundary sliding and diffusion-controlled processes were activated at the higher temperatures.

leading to accommodate deformation. The upper-mentioned thermally activated mechanism decreases the resistance against plastic deformation and increases the strain rate sensitivity at elevated temperatures (Fig. 6). Hence, the strain rate sensitivity increases with temperature and improves the material's ability to distribute stress uniformly during deformation. Figure 7 (a), Fig. 7 (b), Fig. 7 (c), Fig. 7 (d) and Fig. 7 (e) shows the variation in strain rate sensitivity (m) during the change in temperature with the help of contour plots at 0.02, 0.04, 0.06, 0.08 and 0.10 strain respectively. Further, the result revealed that the strain rate sensitivity (m) was increased with the increase in temperature. In the contours plot, red and blue colors exhibited the maximum and minimum values of m respectively. The maximum strain rate sensitivity was observed at 1000℃ and the strain rate ranged 10^{-3} to 10° s^{-1} for all the strain values 0.02, 0.04, 0.06, 0.08 and 0.10.

The power dissipation efficiency (η) was estimated with the help of Eq. (12). Further, the equation shows the dependency of strain rate sensitivity on the power dissipation efficiency

(η). Figure 8 shows the effect of temperature and strain rate on the power dissipation efficiency (η) at the different strain values 0.02, 0.04, 0.06, 0.08 and 0.10. The results revealed that the power dissipation efficiency

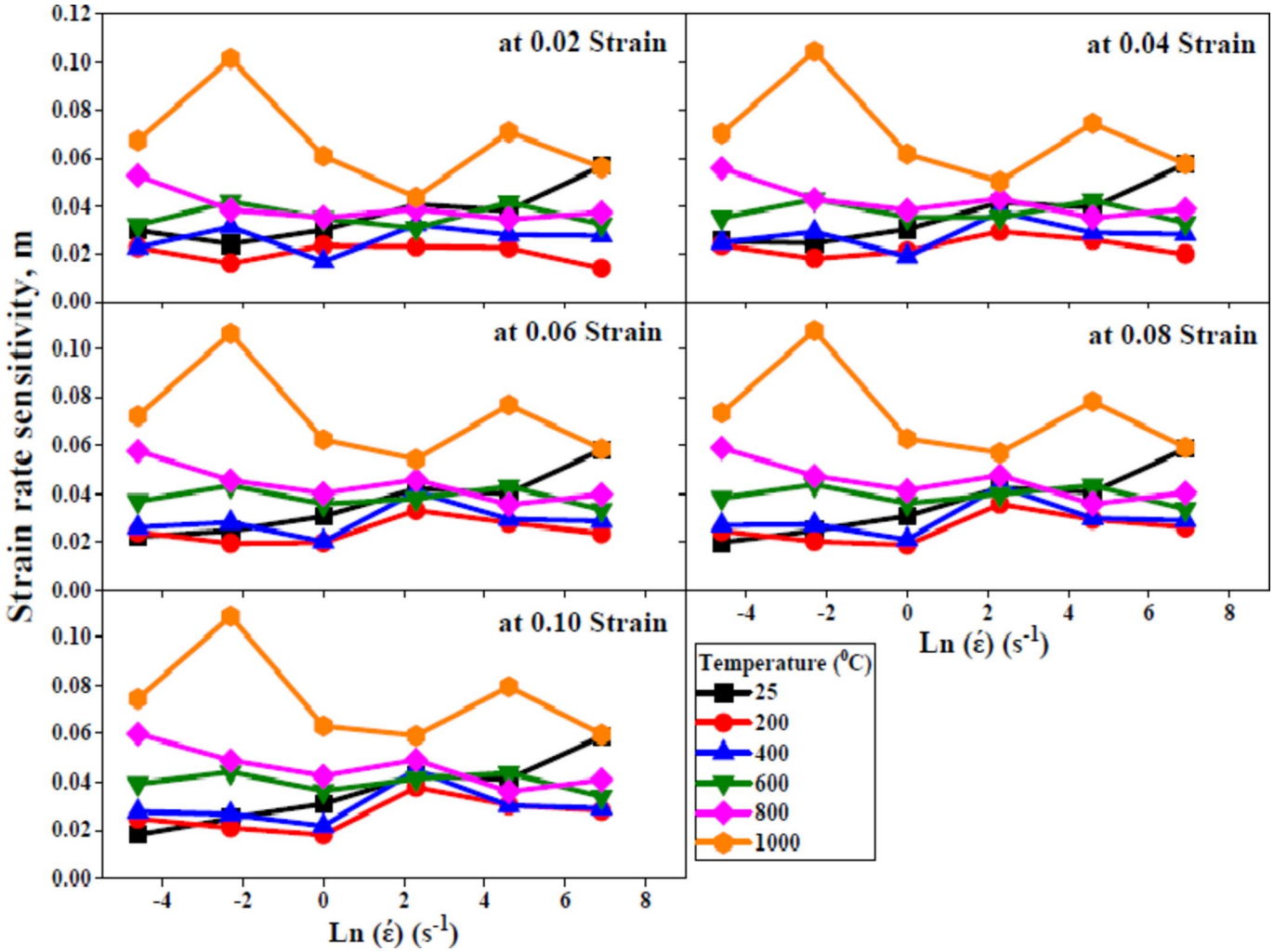

Fig. 6. Variation in strain rate sensitivity (m) with temperature, strain and strain rate for SLM 3D printed SS316L steel.

was increased with the increase in the temperature for all the strain rate ranges 10^{-3} to $10^{3}s^{-1}$. The temperature directly influenced the material's energy dissipation ability during deformation.

The thermally activated deformation mechanisms like dislocation climb, cross-slip, and grain boundary sliding become more prominent at elevated temperatures Further, the deformation mechanism reduces the material's resistance to plastic deformation. This facilitates greater energy dissipation through dynamic recrystallization or recovery and leads to an increase in power dissipation efficiency. The dominance of strain hardening and limited activation of these mechanisms result in reduced energy dissipation at lower temperatures which results in lowering η. Hence, power dissipation efficiency improves at elevated temperatures which reflects the material's enhanced deformation accommodation ability during energy-absorbing processes. The power dissipation efficiency (η) increases with the increase in strain rate up to 600℃. A zig-zag region was observed after the 600℃ for all the strain values. Figure 9 (a), Fig. 9 (b), Fig. 9 (c), Fig. 9 (d) and Fig. 9 (e) shows the power dissipation efficiency (η) map contours at the strain of 0.02, 0.04, 0.06, 0.08 and 0.10 respectively. Further, the result revealed that peak efficiency was achieved at the highest temperature 1000℃. The results also exhibited a good efficiency zone at the 800℃ to 1000℃ temperature range. The strain rate influenced the activation of deformation mechanisms. The thermally assisted processes (dynamic recrystallization, recovery, and grain boundary sliding) have sufficient time to occur at low strain rates resulting in enhancing η. Further, the high strain rates limit the activation of the above-mentioned mechanisms which results in increased strain hardening and reduced energy dissipation. This results in a lower η at higher strain rates, as more energy is stored elastically rather than dissipated. Therefore, η typically decreases as the strain rate increases.

Effect of different parameters on the instability dimensionless parameter ($\xi\ (\dot{\epsilon})$)

The values of the instability dimensionless parameter ($\xi\ (\dot{\epsilon})$) was calculated with the condition mentioned in the Eq. (13). Equation (13) shows the dependency of $\xi\ (\dot{\epsilon})$ on the strain rate sensitivity (m) and the strain rate. Only negative values of $\xi\ (\dot{\epsilon})$ has been considered to show the instability region for hot working of SLM 3D printed SS316L steel. Figure 10 shows the variation of $\xi\ (\dot{\epsilon})$ with the variation in strain rate, temperature

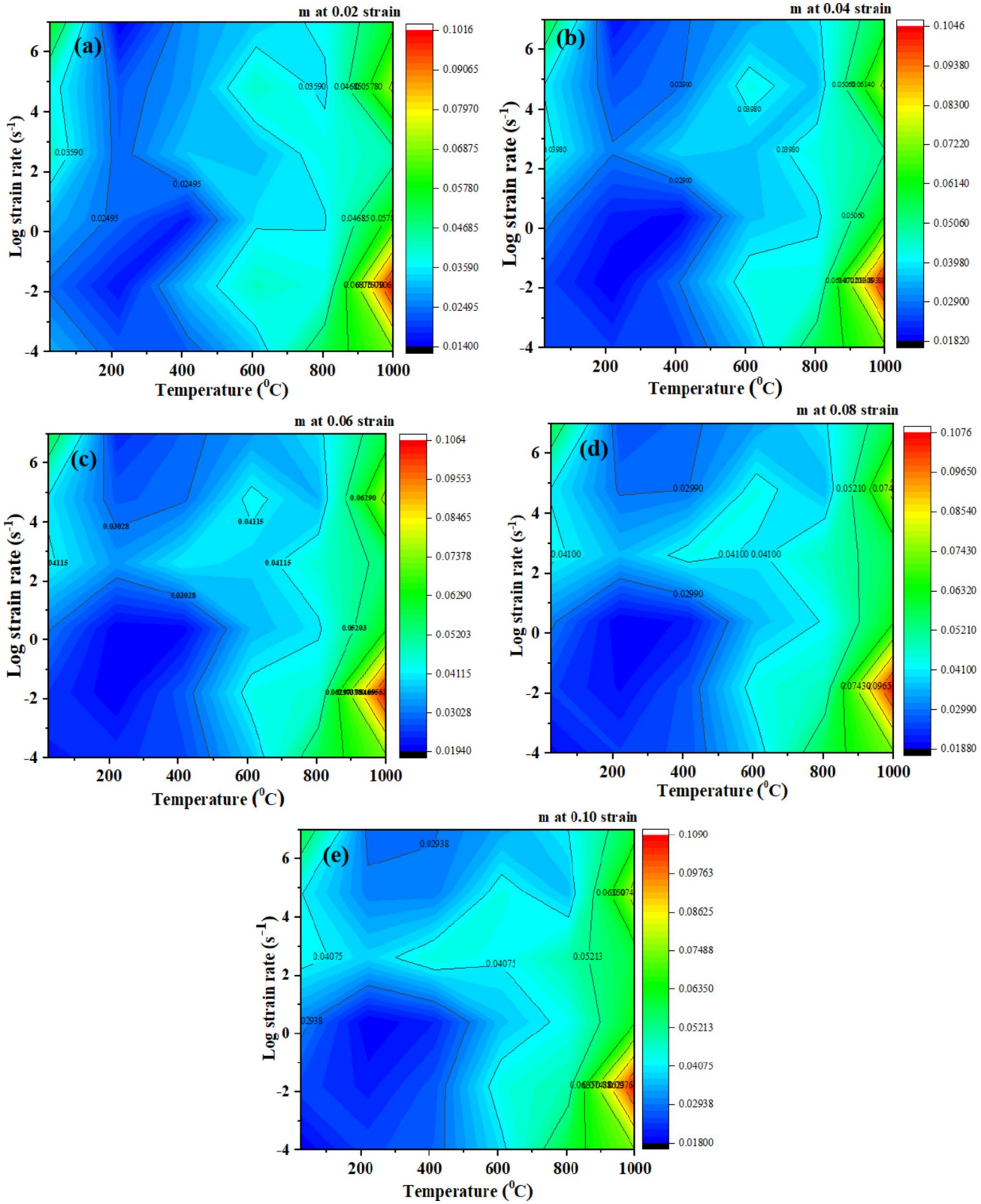

Fig. 7. Strain rate sensitivity contours at different strain (**a**) 0.02, (**b**) 0.04, (**c**) 0.06, (**d**) 0.08 and (**e**) 0.10

and strain. Further, the result revealed that the negative values of $\xi\ (\dot{\epsilon})$ is considered for the representation of instability. The maximum instability occurred at the strain rate of $10^0\ s^{-1}$ and $10^1\ s^{-1}$ strain rate. Further, the.

instability occurred at 25, 200, 400 and 800℃ for all the strain values. Figure 11 (a), Fig. 11 (b), Fig. 11 (c), Fig. 11 (d) and Fig. 11 (e) shows the $\xi\ (\dot{\epsilon})$ map contours at the strain of 0.02, 0.04, 0.06, 0.08 and 0.10

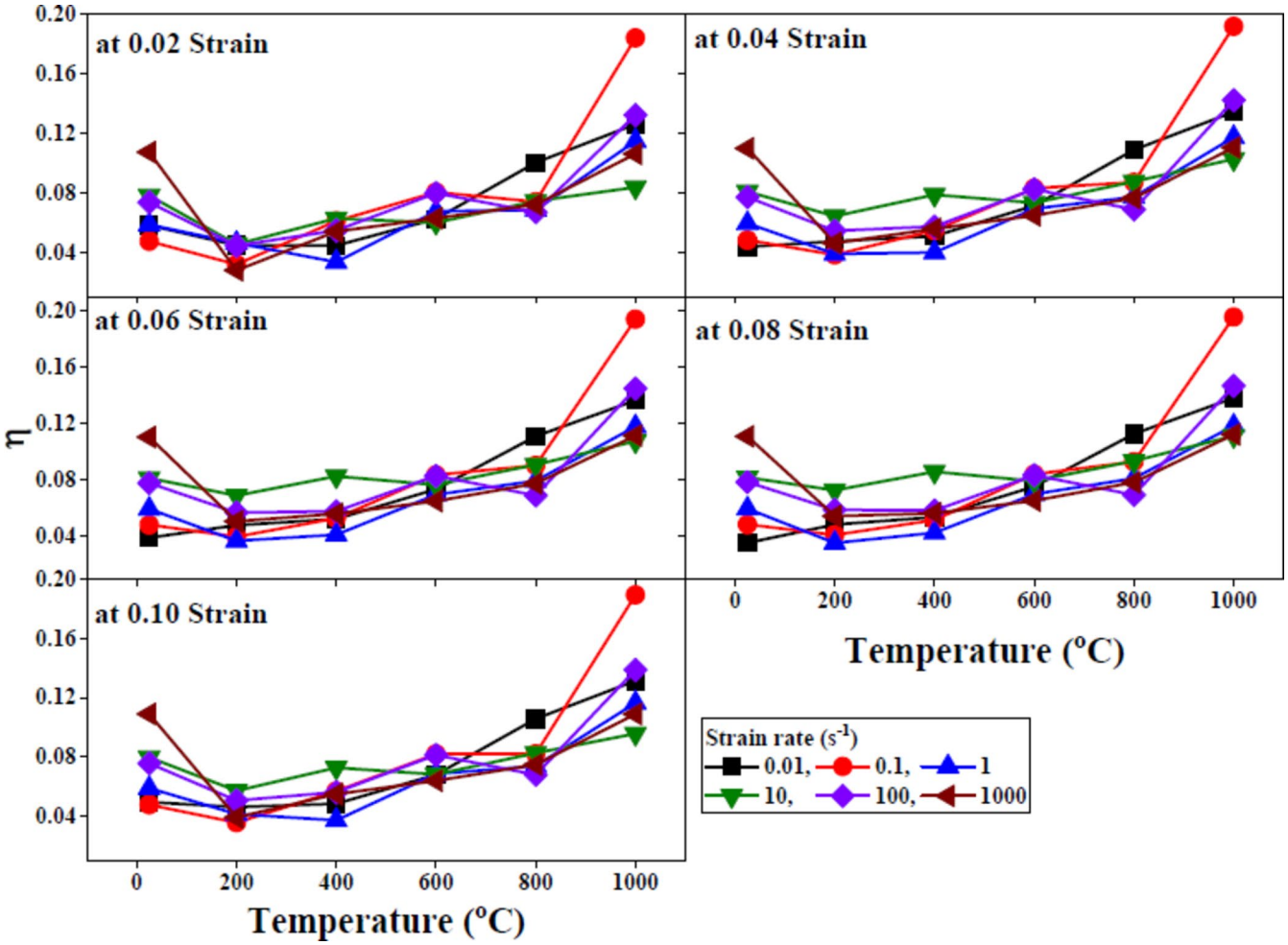

Fig. 8. Power dissipation efficiency (η) at varying strain rates and strains.

respectively. The negative values of yellow and red regions exhibited the instability region for SLM 3D printed SS316L steel at all the mentioned strain values.

Processing maps for SLM 3D printed SS316L steel

Figure 12 (a), Fig. 12 (b), Fig. 12 (c), Fig. 12 (d) and Fig. 12 (e) show the SLM 3D printed SS316 L steel processing maps at 0.02, 0.04, 0.06, 0.08 and 0.10 respectively. The processing maps were established to overlap the instability map on the power dissipation efficiency map. In Fig. 12 (a-e) the shaded area represents the instability region and the black-lined white region represents the power dissipation efficiency area. Further, the results revealed that the instability region was increased with the increase in strain values. The highest power dissipation efficiency of 18% has occurred at the elevated temperature range 800℃–1000℃ and low strain rate range 10^{-2} – 10^{-1} s^{-1} (at the 0.02, 0.04, 0.06, 0.08 and 0.10 strain). Further, the unsafe instability region occurred at the low strain rate range (10^{-2} – 10^{-1} s^{-1}), high strain rate range (10^{2}–10^{3} s^{-1}) and temperature range (200–400^{0} C, and 800 – 100℃) for 0.02, 0.04, 0.06, 0.08 and 0.10 strain. The hot processing safe zone for SLM 3D printed SS316L occurred at the elevated temperature range 800–1000℃ and low strain rate range 10^{-2} – 10^{-1} s^{-1} (at the 0.02, 0.04, 0.06, 0.08 and 0.10 strain). Furthermore, the hot working unsafe zone for SLM 3D printed SS316L occurred within the shaded area in Fig. 12 (a-e) at 0.02, 0.04, 0.06, 0.08 and 0.10 strain. The current investigation deals with the generation of hot working processing maps by superimposing the instability dimensionless parameter ($\xi(\dot{\varepsilon})$) map on the power dissipation efficiency (η) map for SLM 3D-printed SS316L steel. The processing maps provide significant insights into the material's deformation behavior at elevated temperatures which helps to select stable and unstable processing zones. The power dissipation efficiency map reflects the ability of the material to undergo dynamic restoration mechanisms (recrystallization), while the instability parameter map highlights regions prone to flow localization, cracking, or void formation defects. An optimal processing window was identified to enhance mechanical properties, improve formability, and reduce residual stresses by combining these maps. Further, the used approach is particularly valuable for additive-manufactured components, where microstructural anisotropy and porosity influence hot working behavior. The results of current investigation help in the selection of appropriate temperature and strain rate conditions, to ensure defect-free processing

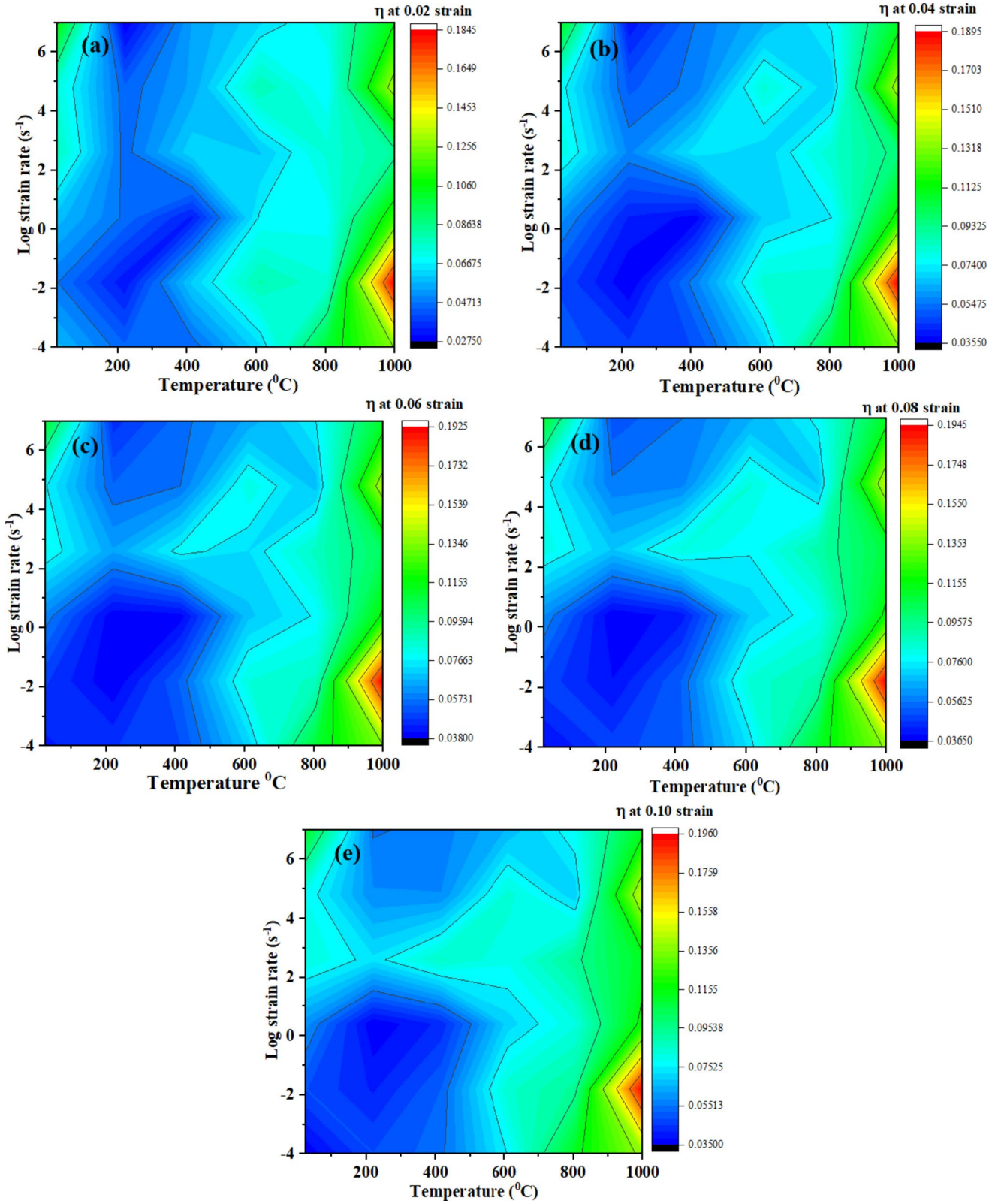

Fig. 9. Power dissipation efficiency (η) map contours at different strains (**a**) 0.02, (**b**) 0.04, (**c**) 0.06, (**d**) 0.08 and (**e**) 0.10.

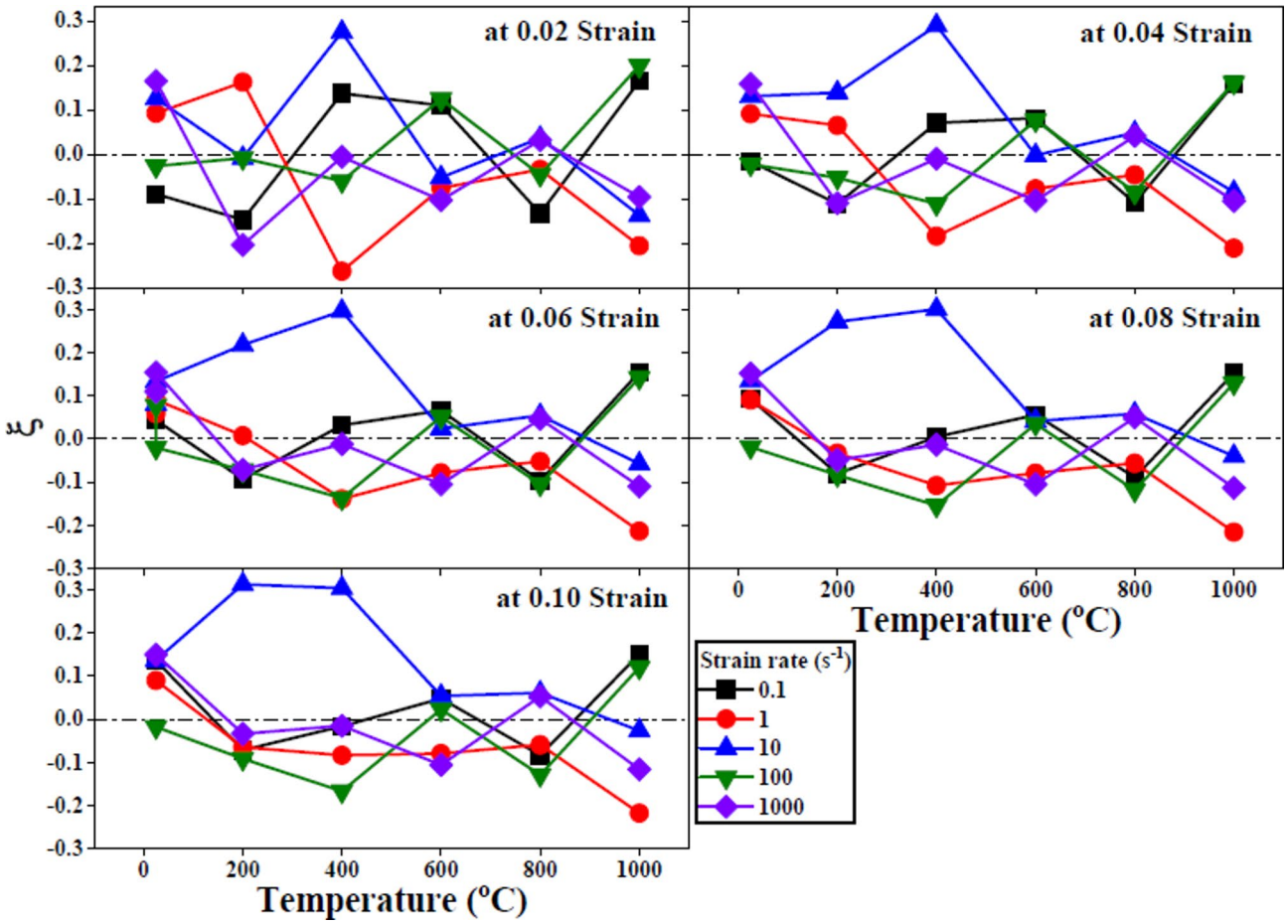

Fig. 10. Instability dimensionless parameter ($\xi\ (\dot{\epsilon})$) at different strain rates and strains.

and enhanced performance of SS316L parts in industries such as aerospace, biomedical, and automotive manufacturing.

One major constraint during the present investigation is the limited strain rate and temperature range (10^{-3}–10^{3} s^{-1} and 25–1000 °C) used in the experiments. Further, the used ranges are relevant for many industrial, aerospace and bio-medical applications but do not fully capture extreme conditions encountered in specialized manufacturing processes such as high-speed forging or superplastic forming. Further, the study assumes homogeneous plastic deformation throughout the material, which may not accurately represent real-world scenarios where localized strain variations, grain size effects, and thermal gradients can impact workability. The second limitation is the lack of in-situ microstructural analysis during deformation as it prevents direct observation of phase transformations, grain refinement, and defect formation. The conduction of in-situ high-temperature deformation experiments, expanding the processing window, and incorporating finite element simulations to enhance predictive capabilities can be done for future studies.

The SLM 3D printed SS316L steel scanning electron microscopy (SEM) micrograph has been shown in Fig. 13 (a) and Fig. 13 (b) at the $10^{-3}s^{-1}$ and 10^{3} s^{-1} strain rates respectively for room temperature. Further, Fig. 13 (c) and Fig. 13 (d) at the $10^{-3}s^{-1}$ and 10^{3} s^{-1} strain rates respectively for 1000^{0}C temperature. Figure 13 (a) and Fig. 13 (b) show the quasistatic deformation crack and high deformation crack at $10^{-3}s^{-1}$ and 10^{3} s^{-1} strain rates for room temperature. The cracks did not much appear at the low strain rate ($10^{-3}s^{-1}$) quasistatic deformation but at the high strain rate (10^{3} s^{-1}) deformation, a visible number of cracks appeared in the SEM micrograph. Further, the micrograph revealed that internal cracks are formed at elevated temperature and low strain rates which leads to instability region as shown in Fig. 11 (a-e) and Fig. 12 (a-e). Further, 13 (c) shows that at 1000℃ temperature and 10^{-3} s^{-1} strain rate grain boundary are expand and increase the hot deformation workability and power dissipation efficiency (η) (as shown in Fig. 9 (a-e) and Fig. 12 (a-e)).

Effect of temperature on the hardness of SLM 3D printed SS316L specimen

The SLM 3D-printed SS316L stainless steel hardness was decreased progressively with increasing temperature due to microstructural changes developed by thermal conditions. Figure 14 shows the variation in Vicker's hardness against temperature. Further, the results revealed that the specimen exhibits a high hardness of 237 HV at room temperature, attributed to its fine-grained microstructure, high dislocation density, and residual stresses retained from the rapid solidification during the selective laser melting process. The hardness slightly decreased

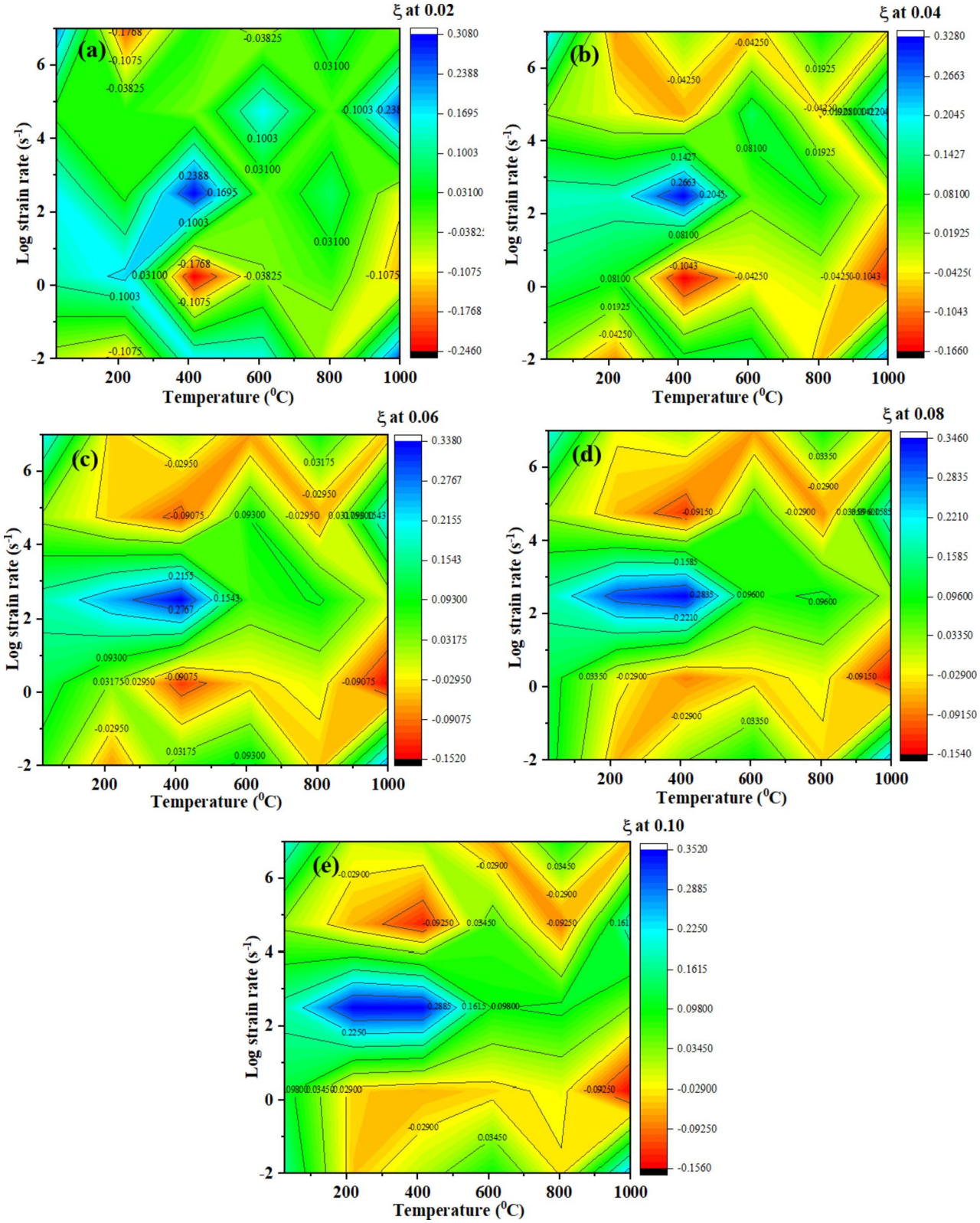

Fig. 11. Instability dimensionless parameter ($\xi\ (\dot{\epsilon})$) contours at strain values (**a**) 0.02, (**b**) 0.04, (**c**) 0.06, (**d**) 0.08 and (**e**) 0.10.

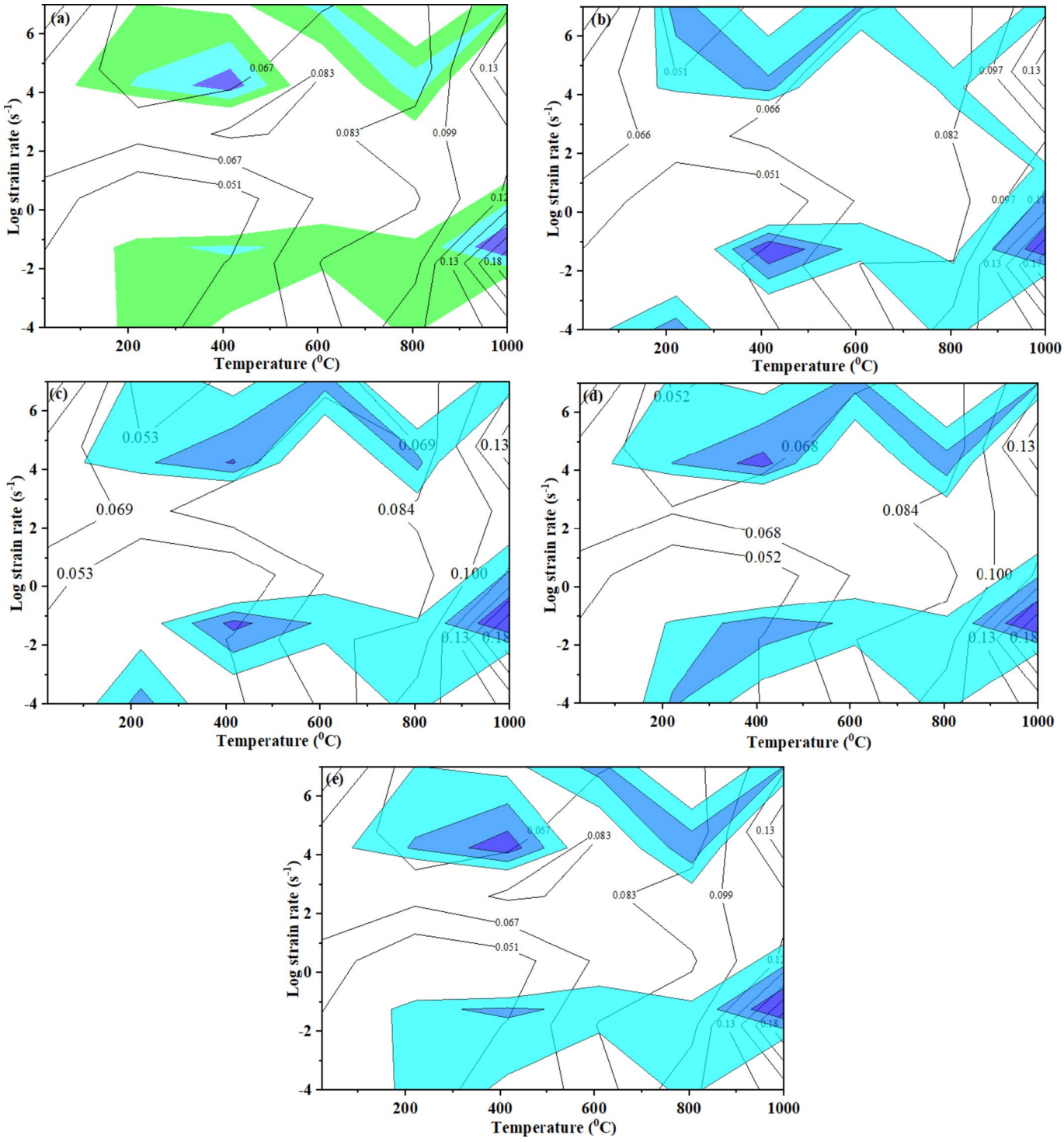

Fig. 12. Processing maps for SLM 3D printed SS316L steel at strain values (**a**) 0.02, (**b**) 0.04, (**c**) 0.06, (**d**) 0.08 and (**e**) 0.10.

to 228 HV at 200 °C due to the relaxation of residual stresses and minor recovery of dislocations. The hardness further drops to 209 HV at 400 °C due to the diffusion-driven processes facilitates dislocation annihilation and slight grain coarsening. A more significant reduction to 190 HV at 600 °C has been observed corresponding to the initiation of recrystallization, where new strain-free grains begin to form, reducing the strengthening effects of dislocations. The hardness deceases further to 171 HV at 800 °C due to extensive grain growth and the dissolution of fine cellular structures which contributed to strength. Further, the hardness decreases up to 152 HV at 1000 °C, exhibited softening due to complete recrystallization, enlarged microstructure, equiaxed grains with reduced dislocation density which reduces the material hardness and strength.

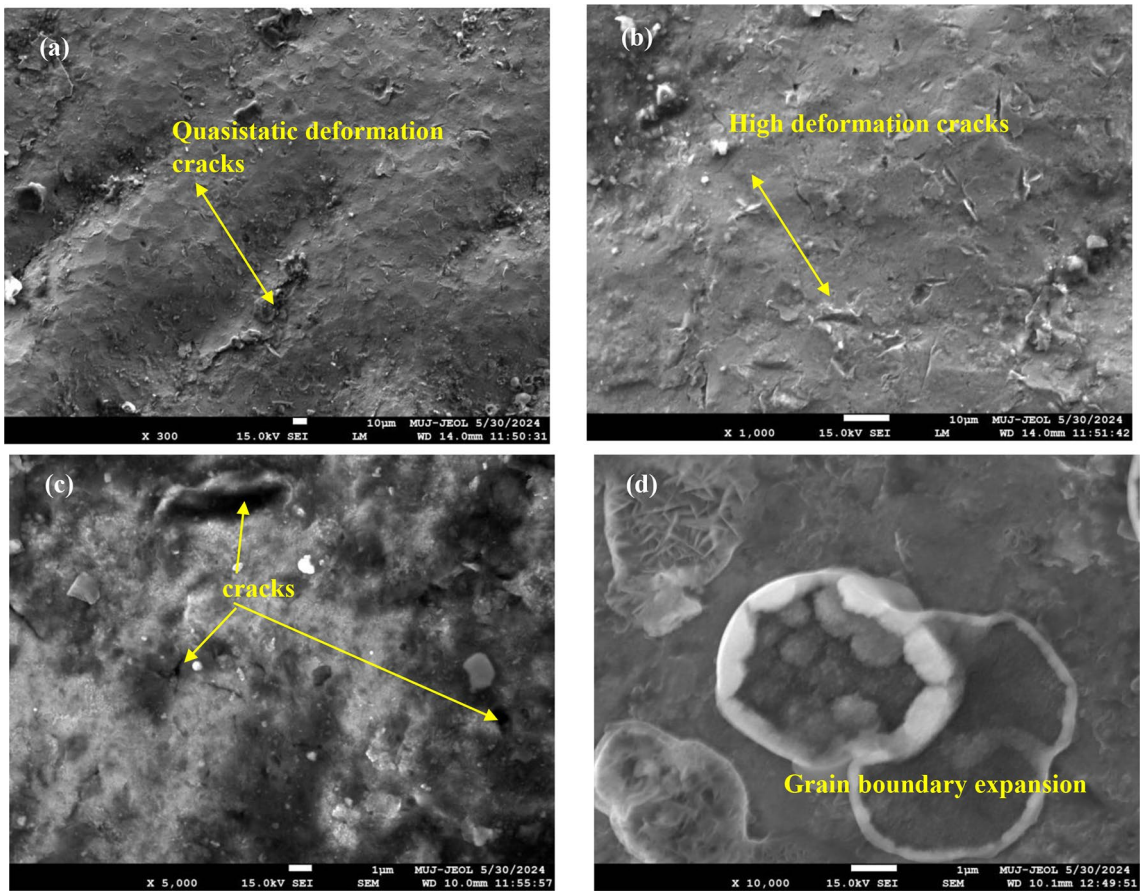

Fig. 13. Scanning electron micrograph for SLM 3D printed SS316L steel at room temperature (**a**) $10^{-3}s^{-1}$ strain rate, (**b**) 10^{3} s^{-1} strain rate and at 1000^{0}C (**a**) $10^{-3}s^{-1}$ strain rate, (**b**) 10^{3} s^{-1} strain rate.

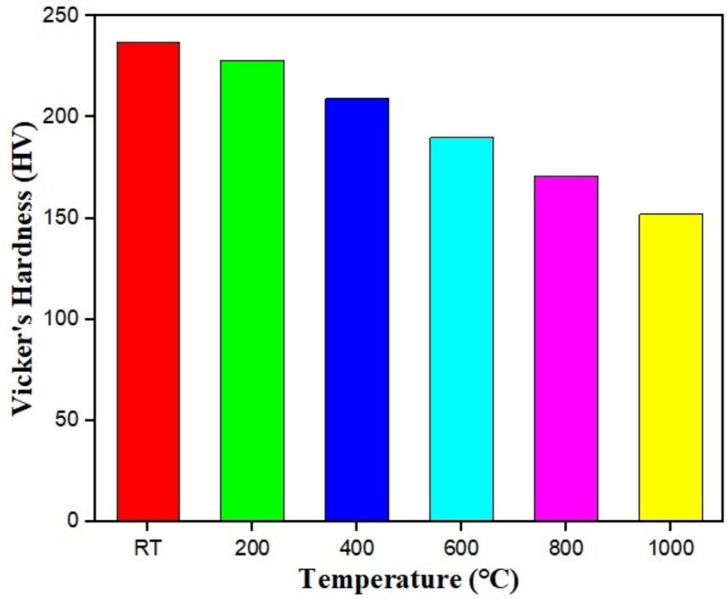

Fig. 14. Vicker's hardness of SLM 3D printed specimen at elevated temperatures.

Conclusions

The following conclusion has been drawn from the current investigation:

i. The strain rate sensitivity (m) of the SLM 3D printed SS316L steel was increased with the increase in the temperature at each plastic strain value (0.02, 0.04, 0.06, 0.08 and 0.10).
ii. The increase in temperature increases the thermal energy in the material and leads to dislocation mobility which is the main cause of deformation accommodation in the investigated material.
iii. The maximum strain rate sensitivity was observed at 1000^0C and the strain rate ranged 10^{-3} to 10^0 s^{-1} for all the strain values 0.02, 0.04, 0.06, 0.08 and 0.10.
iv. The peak power dissipation efficiency (η) was achieved at the highest temperature 1000℃ and 10^{-1} s^{-1} strain rate.
v. The maximum instability (ξ $(\dot{\epsilon})$) occurred at the strain rate of 10^0 s^{-1} strain rate and 1000^0C temperature for all the strain values.
vi. The unsafe instability region occurred at the low strain rate range (10^{-2} – 10^{-1} s^{-1}), high strain rate range (10^2–10^3 s^{-1}) and temperature range (200–400℃, and 800 – 100℃) for 0.02, 0.04, 0.06, 0.08 and 0.10 strain. Further, the remaining area was useful for hot workability.
vii. The micrograph revealed that internal cracks are formed at the elevated temperature and low strain rates which leads to instability region. Further, the expansion of grain boundaries at elevated temperature increases the hot deformation workability of the SLM 3D printed SS316L steel.
viii. The Vicker's hardness for room temperature was observed as 237 HV. Further, the hardness was decreased with 3.87%, 12.55%, 22.01%, 32.35%, and 43.70% at 200^0C, 400^0C, 600^0C, 800^0C and 1000^0C respectively.
ix. The reduction in hardness exhibited softening due to complete recrystallization, enlarged microstructure, equiaxed grains with reduced dislocation density which decrease the material hardness and strength.

Ethics declarations.

Conflict of interest /Competing interests: The authors declare no competing interests.

Data availability

All data generated or analysed during this study are included within this manuscript. All the characterizations, analysis, testing's related work and testing's has solely been responsible by Ambuj Saxena. Additionally, the raw data can be obtained on request from one of the corresponding author, Ambuj Saxena.

Received: 10 December 2024; Accepted: 26 March 2025
Published online: 09 May 2025

References

1. Saxena, A., Srivastava, A. K., Kushwaha, P. K. & Sharma, S. An investigation on the influence of three-dimensional printing orientation on the tensile and flexural strength of polymer and plastic materials. *Mech. Adv. Mater. Struct.*, **31**, pp.1–12. (2024).
2. Suryawanshi, J., Prashanth, K. G. & Ramamurty, U. Mechanical behavior of selective laser melted 316L stainless steel. *Mater. Sci. Engineering: A*. **696**, 113–121 (2017).
3. Gustmann, T. et al. Influence of processing parameters on the fabrication of a Cu-Al-Ni-Mn shape-memory alloy by selective laser melting. *Additive Manuf.* **11**, 23–31 (2016).
4. Wei, Q. et al. Selective laser melting of stainless-steel/nano-hydroxyapatite composites for medical applications: microstructure, element distribution, crack and mechanical properties. *J. Mater. Process. Technol.* **222**, 444–453 (2015).
5. Su, X. & Yang, Y. Research on track overlapping during selective laser melting of powders. *J. Mater. Process. Technol.* **212** (10), 2074–2079 (2012).
6. Attar, H., Calin, M., Zhang, L. C., Scudino, S. & Eckert, J. Manufacture by selective laser melting and mechanical behavior of commercially pure titanium. *Mater. Sci. Engineering: A*. **593**, 170–177 (2014).
7. Wu, W., Yang, Y. & Huang, Y. Direct manufacturing of Cu-based alloy parts by selective laser melting. *Chin. Opt. Lett.* **5** (1), 37–40 (2007).
8. Zhang, X., Chen, L., Zhou, J. & Ren, N. Simulation and experimental studies on process parameters, microstructure and mechanical properties of selective laser melting of stainless steel 316L. *J. Brazilian Soc. Mech. Sci. Eng.* **42**, 1–14 (2020).
9. Murr, L. E. A metallographic review of 3D printing/additive manufacturing of metal and alloy products and components. *Metallography Microstruct. Anal.* **7**, 103–132 (2018).
10. Sun, Z., Tan, X., Tor, S. B. & Yeong, W. Y. Selective laser melting of stainless steel 316L with low porosity and high build rates. *Mater. Design*. **104**, 197–204 (2016).
11. Venugopal, S., Mannan, S. L. & Prasad, Y. V. R. K. Processing map for hot working of stainless steel type AISI 316L. *Mater. Sci. Technol.* **9** (10), 899–906 (1993).
12. Pu, E., Zheng, W., Xiang, J., Song, Z. & Li, J. Hot deformation characteristic and processing map of superaustenitic stainless steel S32654. *Mater. Sci. Engineering: A*. **598**, 174–182 (2014).
13. Wu, Z. et al. *Exploring the influence of Al content on the hot deformation behavior of Fe-Mn-Al-C steels through 3D processing map* Vol. **159**, 447–455 (Vacuum, 2019).
14. Mohamadizadeh, A., Zarei-Hanzaki, A., Abedi, H. R., Mehtonen, S. & Porter, D. Hot deformation characterization of duplex low-density steel through 3D processing map development. *Mater. Charact.* **107**, 293–301 (2015).
15. Mohr, D., Gary, G. & Lundberg, B. Evaluation of stress–strain curve estimates in dynamic experiments. *Int. J. Impact Eng.* **37** (2), 161–169 (2010).
16. Prasad, Y. V. R. K. Recent advances in the science of mechanical processing. *Indian J. Technol.* **28** (6–8), 435–451 (1990).
17. Prasad, Y. V. R. K. Processing maps: A status report. *J. Mater. Eng. Perform.* **12**, 638–645 (2003).
18. Prasad, Y. V. R. K. & Seshacharyulu, T. J. M. R. Modelling of hot deformation for microstructural control. *Int. Mater. Rev.* **43** (6), 243–258 (1998).
19. Prasad, Y. V. R. K. & Seshacharyulu, T. Processing maps for hot working of titanium alloys. *Mater. Sci. Engineering: A*. **243** (1–2), 82–88 (1998).

20. Fu, G. S., Yan, W. D., Chen, H. L., Chen, G. Q. & Cheng, C. Z. Study on hot processing maps and flow instability of 1235 al alloy treated by different methods of purification. *Adv. Mater. Res.* **399**, 1870–1877 (2012).
21. Dieter, G. E. & Bacon, D. *Mechanical metallurgy (Vol* Vol. 3, 43–53 (McGraw-hill, 1976).
22. Bevan, M. A. et al. Mechanical properties and behavior of additive manufactured stainless steel 316L. In *Characterization of minerals, metals, and materials 2017* 577–583 (Springer International Publishing, 2017).
23. Ziętala, M., Durejko, T., Panowicz, R. & Konarzewski, M. Microstructure evolution of 316L steel prepared with the use of additive and conventional methods and subjected to dynamic loads: a comparative study. *Materials*, **13**(21), p.4893. (2020).
24. Chen, J. et al. Dynamic mechanical properties of 316L stainless steel fabricated by an additive manufacturing process. *J. Mater. Res. Technol.* **11**, 170–179 (2021).
25. Kneen, T. J. et al. Mechanical behaviour and high strain rate deformation of stainless steel 316L processed by selective laser melting. *Int. J. Rapid Manuf.* **9** (1), 84–103 (2020).
26. Gupta, M. K. et al. Fabrication and investigation of mechanical behaviors of TiB2 reinforced AMCs. *Trans. Indian Inst. Met.* **77** (2), 563–570 (2024).
27. Rahman, M. S., Sattar, N. S., Ahmed, R. U., Ciaccio, J. & Chakravarty, U. K. A machine learning framework for Melt-Pool geometry prediction and process parameter optimization in the laser Powder-Bed fusion process. *J. Eng. Mater. Technol.* **146**(4), 041006, pp.1–40. (2024).
28. Rahman, M. S., Schilling, P. J., Herrington, P. D. & Chakravarty, U. K. Thermofluid properties of Ti-6Al-4V melt pool in powder-bed electron beam additive manufacturing. Journal of Engineering Materials and Technology, **141**(4), p.041006. (2019).

Acknowedgements
The authors extend their appreciation to the Deanship of Scientific Research at King Khalid University for funding this work through large group Research Project under grant number RGP2/28/44.

Author contributions
Conceptualization, Ambuj Saxena, Shashi Prakash Dwivedi, Neeraj Mishra, Tarun Kumar Gupta, N. Beemkumar, Ankit Kedia; methodology, Ambuj Saxena, Shashi Prakash Dwivedi, Neeraj Mishra, Tarun Kumar Gupta, N. Beemkumar, Ankit Kedia; formal analysis, Ambuj Saxena, Shashi Prakash Dwivedi, Shubham Sharma, Neeraj Mishra, Tarun Kumar Gupta, N. Beemkumar, Ankit Kedia; investigation, Ambuj Saxena, Shashi Prakash Dwivedi, Neeraj Mishra, Tarun Kumar Gupta, N. Beemkumar, Ankit Kedia; writing—original draft preparation, Ambuj Saxena, Shashi Prakash Dwivedi, Neeraj Mishra, Tarun Kumar Gupta, N. Beemkumar, Ankit Kedia; writing—review and editing, Shubham Sharma, V Nagabhushana Rao, Ehab El Sayed Massoud, Dražan Kozak, Jasmina Lozanovic; supervision, V Nagabhushana Rao, Ehab El Sayed Massoud, Dražan Kozak, Jasmina Lozanovic; project administration, V Nagabhushana Rao, Ehab El Sayed Massoud, Dražan Kozak, Jasmina Lozanovic; funding acquisition, V Nagabhushana Rao, Ehab El Sayed Massoud, Dražan Kozak, Jasmina Lozanovic. All authors have read and agreed to the published version of the manuscript.

Funding
The authors extend their appreciation to the Deanship of Scientific Research at King Khalid University for funding this work through large group Research Project under grant number RGP2/28/44.

Declarations

Conflict of Interests/Competing interests
The authors declare no competing interests.

Ethical approval
Not applicable.

Consent to participate
Not applicable.

Consent to publish
All authors have read and approved this manuscript.

Additional information
Correspondence and requests for materials should be addressed to S.S. or J.L.

Reprints and permissions information is available at www.nature.com/reprints.

Publisher's note Springer Nature remains neutral with regard to jurisdictional claims in published maps and institutional affiliations.